


Effect of chord-to-diameter ratio on vertical-axis wind turbine wake development

Colin M. Parker¹  · Daniel B. Araya² · Megan C. Leftwich¹

Received: 13 June 2017 / Revised: 25 October 2017 / Accepted: 27 October 2017 / Published online: 9 November 2017
© Springer-Verlag GmbH Germany 2017

Abstract The wake structure of a vertical-axis wind turbine (VAWT) is strongly dependent on the tip-speed ratio, λ , or the tangential speed of the turbine blade relative to the incoming wind speed. The geometry of a turbine can influence λ , but the precise relationship among VAWT geometric parameters and VAWT wake characteristics remains unknown. To investigate this relationship, we present the results of an experiment to characterize the wakes of three VAWTs that are geometrically similar except for the ratio of the turbine diameter (D), to blade chord (c), which was chosen to be $D/c = 3, 6$, and 9 . For a fixed freestream Reynolds number based on the blade chord of $Re_c = 1.6 \times 10^3$, both two-component particle image velocimetry (PIV) and single-component hot-wire anemometer measurements are taken at the horizontal mid-plane in the wake of each turbine. PIV measurements are ensemble averaged in time and phase averaged with each rotation of the turbine. Hot-wire measurement points are selected to coincide with the edge of the shear layer of each turbine wake, as deduced from the PIV data, which allows for an analysis of the frequency content of the wake due to vortex shedding by the turbine.

1 Introduction

Previous work on vertical-axis wind turbines (VAWTs) highlights some of their benefits over larger, more common, horizontal-axis wind turbines (HAWTs), even though a much larger body of literature exists for HAWTs (Ainslie 1988; Barthelmie et al. 2007; Cal et al. 2010; Calaf et al. 2010; Chamorro et al. 2013). Specifically, VAWTs require lower cut-in wind speeds, can be used in smaller spaces, pose minimal threats to migrating birds, and are virtually noiseless (Dabiri 2011; Möllerström et al. 2014).

Previous experimental and computational work on VAWTs has examined the effect of the tip-speed ratio,

$$\lambda = \frac{\omega r}{U_\infty} \quad (1)$$

where ω is the angular blade velocity, r is the turbine radius and U_∞ is the incoming wind velocity, on the VAWT wake development. This parameter, the ratio between the blade speed and the free-stream velocity, has been shown to dominate the structure of the turbine's wake (Barsky et al. 2014; Edwards et al. 2015; Posa et al. 2016; Parker and Leftwich 2016; Ryan et al. 2016; Roh and Kang 2013). As tip-speed ratio increases, each VAWT sees a smaller range of effective angle of attack. This plays a critical role in the wake dynamics affecting the dynamic stall of the blades (Dunne and McKeon 2015; Simão Carlos et al. 2009). Additionally, as the blades rotate faster relative to the freestream, this incoming flow has less time to adjust to the passing blades. This has the effect of making a VAWT appear more solid to the incoming flow than it would be based solely on its geometry, which is an effect that can be quantified by wake measurements.

✉ Colin M. Parker
colinparker@gwu.edu

Daniel B. Araya
dbaraya@central.uh.edu

Megan C. Leftwich
mleftwich@gwu.edu

¹ Department of Mechanical and Aerospace Engineering, The George Washington University, Washington DC, USA

² Department of Mechanical Engineering, University of Houston, Houston, TX, USA

The geometric solidity of the turbine, σ is defined as

$$\sigma = \frac{nc}{\pi D} \quad (2)$$

where c is the blade chord length, D is the turbine diameter, and n is the number of blades. In our experiment, we varied the parameter D/c to change the geometric solidity among the models. The effect of varying geometric solidity on the turbine performance has been reported in previous studies (Howell et al. 2010; Roh and Kang 2013). Recently, it was shown that the energy efficiency could be optimized based on the ratio of D/c (Bianchini et al. 2015).

Araya et al. (2017) investigated characteristics of the VAWT wake due to changes in an effective turbine solidity which they defined by a parameter called the ‘dynamic solidity’, σ_D , where,

$$\sigma_D = 1 - \frac{1}{2\pi\sigma\lambda} \quad (3)$$

The physical interpretation of σ_D is of how ‘solid’ the turbine appears to the flow relative to a stationary cylinder of the same diameter. They observed that the dynamics in the VAWT wake can be characterized by a near-wake region dominated by blade-scale vortices, followed by a transition to large-scale velocity fluctuations in the far wake similar to a bluff body. Furthermore, σ_D was found to be highly correlated to the start of the far-wake transition, which indicated its predictive value.

In this work, we provide new experimental data to test the findings of Araya et al. (2017) and also to explore unanswered questions about VAWT wake development. By creating three turbines with varied diameters, we are changing the geometric solidity of the VAWT in a new way. Wake profiles are compared when changing the dynamic solidity via this chord to diameter ratio while the tip-speed ratio is held constant. Then we explore the persistence of vortices shed from the blades in the near wake. By looking at the decay of these vortices, we can compare the start of a wake transition over a range of dynamic solidity and tip-speed ratios.

2 Experimental setup and methods

2.1 Turbine models and test facility

The model turbines are small-scale, straight-blade, Darrieus-type vertical-axis wind turbines. They consist of three symmetric NACA 0022 airfoils mounted at 120° intervals around a shaft (see Fig. 1). Dynamic parameters, tip-speed ratio and Reynolds number, are shown in Table 1. The chord Reynolds number is set to $Re_c = 1.6 \times 10^3$, resulting in different Re_D for each model. While the maximum Reynolds number in these experiments is below where the power

curves are Reynolds number independent (Armstrong et al. 2012), the wake velocity profiles in this range are not very sensitive to this difference (Parker and Leftwich 2016). Geometrically, we are limited by the height of our wind tunnel, forcing the height-to-diameter ratio to be low. While aspect ratio and three-dimensional effects do play a part in turbine performance (Brusca et al. 2014; Tescione et al. 2014), our focus is on the dominant dynamics in the wake, which can be characterized by planar measurements (Araya et al. 2017). In our experimental setup, the turbine spans 80% of the test section and we see minimal three-dimensional effects at the midsection (Parker and Leftwich 2016).

Both the blades and struts are 3D printed with a Fortus 250 mc 3D printer (Proto3000, Vaughan, ON). These are then painted black and sanded to reduce reflections and smooth the surface. The struts are connected to the blades using plastic epoxy and the blade strut assembly is then screwed into the shaft. This allows the three models to be easily changed without removing the mounted drive shaft assembly from the wind tunnel. Each model has three blades ($n = 3$), each with a chord length of $c = 5$ cm. The three models are created with different geometric solidities. To vary to solidity (defined by Eq. 2), the diameter of the turbine (i.e., length of the strut connecting the blades to the shaft) is varied. By printing different length struts, the diameter is changed to create models with ratios of $D/c = 3, 6$ and 9. A computer-aided design (CAD) model of the turbines is shown in Fig. 1.

The models are mounted in the test section [0.91 m (width) \times 0.36 m (height) \times 2.44 m (length)] of a low-speed wind tunnel. We can compare the blockage effect of the different models by taking the frontal projected area of the turbine (i.e., area normal to the freestream velocity) divided by the cross-sectional area of the test section. For the smallest turbine, with a ratio of $D/c = 3$, the maximum blockage in the rotation cycle is 9% with a minimum of 6% blockage. When increasing the turbine diameter to the maximum value of $D/c = 9$, the projected blockage ranges from 7 to 11% (note that the boundary layer on the walls of the tunnel is of negligible thickness at these experimental conditions). This increase is due to the added strut length, but the effective blockage is similar among the turbines. Additionally, we can compare wall effects between the turbines as the diameter is varied between models. The distance from the wall varied from 0.38 m (2.5 D) for $D/c = 3$ to 0.23 m (0.51 D) for $D/c = 9$. We do see some flow acceleration around the turbines creating wake compression downstream which is consistent with previous work (Battisti et al. 2011).

The freestream velocity was set to achieve a sufficiently high Reynolds number for wake similarity (as in Parker and Leftwich 2016). The length scale was set based on the chord length c to give a constant Re_c among the models; thus the freestream velocity of the tunnel is consistent for all tests,

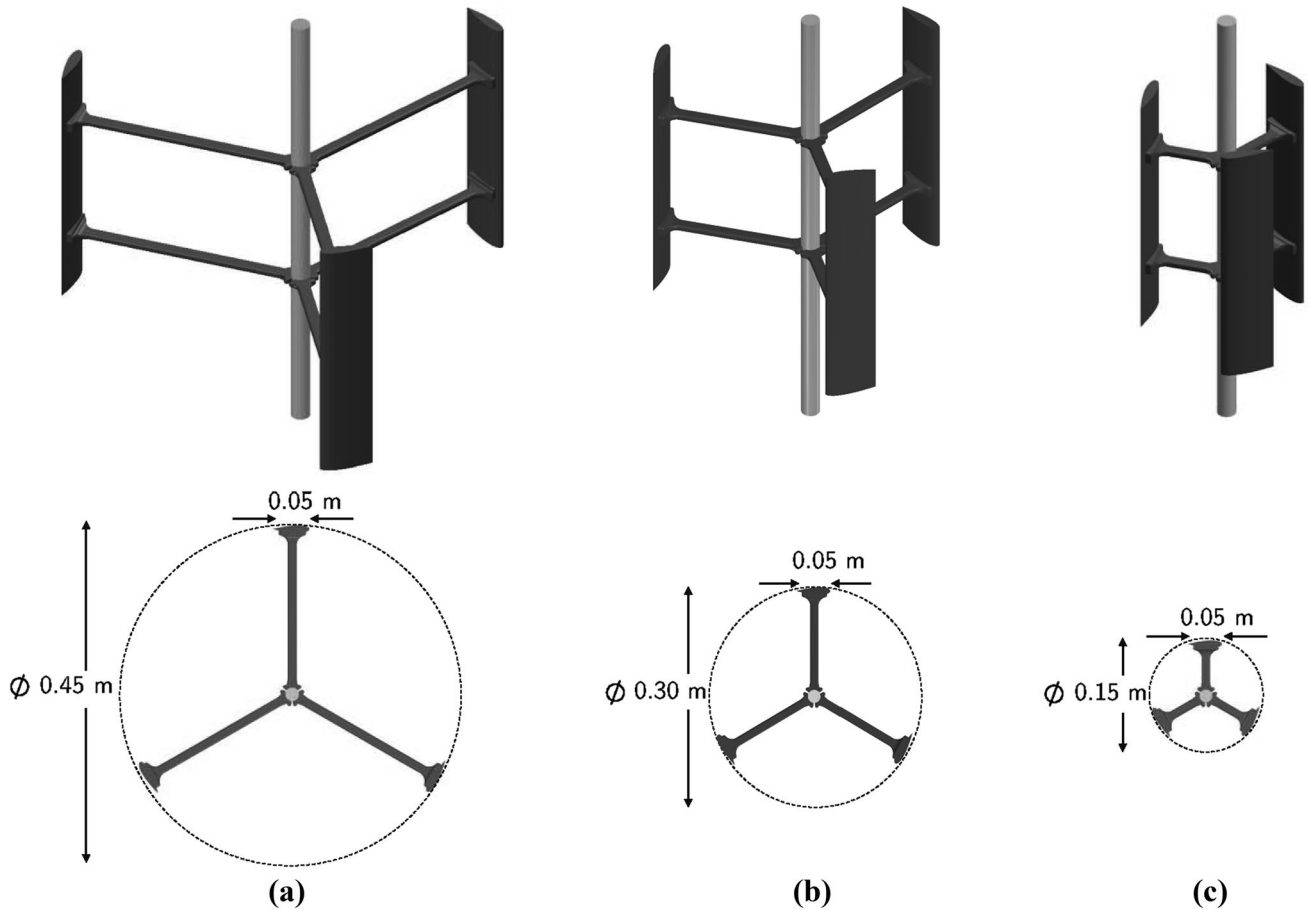


Fig. 1 Three models of 3D printed turbines are shown above. The chord length is constant at $c = 0.05$ m. The diameter, and subsequently the D/c ratio, is varied by changing the strut length. The

above turbines from left to right have ratios of **a** $D/c = 3$, **b** $D/c = 6$, and **c** $D/c = 9$. The turbine height is restricted by the tunnel and is set to $H = 0.305$ m

Table 1 VAWT parameters

Parameter	Model
Reynolds number by diameter (Re_D)	$(0.5, 1.0, 1.5) \times 10^5$
Reynolds number by chord (Re_c)	1.6×10^3
Tip-speed ratio (λ)	1.3, 0.3–2.0 ^a
Chord-to-diameter ratio (D/c)	3 6 9

^a $\lambda = 1.3$ was used for PIV, while CTA measurements spanned $\lambda = 0.3$ –2.0

unavoidably creating different values of Re_D for the different turbines. While over a large range of Re_D —certainly up to the full-scale value—this parameter will change the overall wake structure, in the case of the model-scales tested here, this change will not have a drastic effect of the general wake structure.

To directly control the tip-speed ratio, the turbines are driven by a stepper motor system. The system is controlled through Labview using an NI-USB 6343 I/O

board (National Instruments, Austin, TX, USA). The drive system is monitored using an optical encoder (TRDA-2E360VD, Automation Direct, Cumming, GA, USA) mounted on the through shaft of the motor. The encoder output is used to confirm the rotational velocity, sync the PIV system and provide a reference angle to pair with the hotwire data. However, this measured rate is not used for control because it is not needed. The stepper motor system with open loop control of rotation is accurate to ± 0.01 Hz at low frequency (0–10 Hz) and ± 0.1 Hz at high (10–25 Hz). Thus, the jitter in the system is less than 0.01° when triggering in this method (see Parker and Leftwich (2016) for further details of the experimental methods).

It has been previously shown that a motor-driven turbine can accurately reproduce the physics of a flow-driven turbine when the turbine blades produce net torque due to lift on average, which can be measured either by shaft torque or wake circulation measurements (Araya and Dabiri 2015). For this experiment, the net circulation in the wake of the turbine was calculated from the

time-averaged PIV measurements. It was found that for the conditions of the measured herein, $\lambda \leq 2$, the net circulation in the wake was consistent with that of a flow-driven turbine.

Before we have seen large variation in the wake of VAWT's by varying the tip-speed ratio in a single turbine. In Fig. 2, the dynamic solidity is increased moving along the line for each turbine for an increase in tip-speed ratio. Additionally, at a single tip-speed ratio λ , the dynamic solidity is increased by moving from $D/c = 9$ to $D/c = 3$.

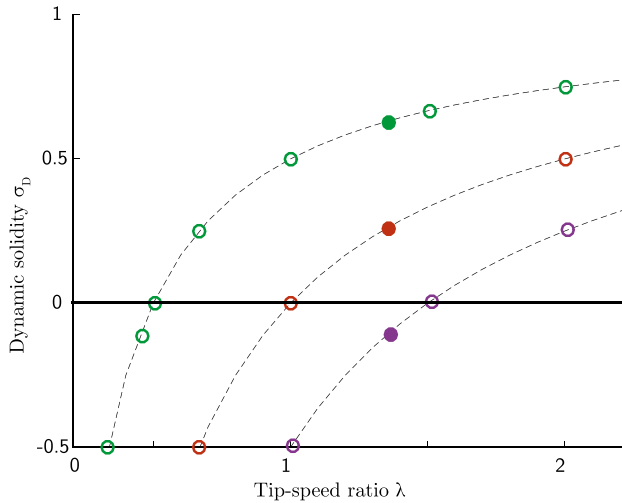


Fig. 2 The parameter space is plotted for the three turbines of $D/c = 3, 6$ and 9 , which correspond to green, red, and purple colored symbols, respectively. The solid points show the values taken for PIV results and the open circles show the CTA results. The region above the solid horizontal line at $\sigma_D = 0$ represents positive dynamic solidity, which is where a turbine is expected to typically operate

2.2 Particle imaging velocimetry

We measure large fields of view in the wake of the turbine with PIV. The flow is seeded with 1 micron particles (aerodynamic diameter) of water-based fog using a Rocket Fogger (LaVision, Inc., Ypsilanti, MI, USA). The particles are illuminated with a 50-50 laser (Litron Lasers, Warwickshire, England) at the horizontal mid-plane behind the turbine. Two Imager sCMOS cameras (LaVision, Inc., Ypsilanti, MI, USA) capture double frame images of the light sheet from above the tunnel.

A pinhole calibration is performed using a LaVision 106-10 calibration plate mounted at the midplane. The location of the origin of the calibration axes are set by a common scaling plate that is 0.9 m (width) \times 2.4 m (length). This is a mounted poster printed with a 1 cm \times 1 cm grid giving a constant reference for each field of view. This allows for all of the fields of view to be combined into the single field that can be seen in Fig. 3. The full field of view is a combination of 16 individual views, with one additional run for the $D/c = 6$ and two for $D/c = 3$ to image closer to the turbine.

Phase averaging is at the rotational rate of the turbine in increments of 10° . For each phase, 250 images are taken and averaged. Due to symmetry, the phase averaged results are taken through one-third of a rotation. The PIV timing unit is synced to the rotation of the turbine using the optical encoder which updates the frequency once per rotation. A time delay is then used to progress through the different phases of the rotation.

To take a time average of the flow, the system is synced to trigger images proceeding 1 degree per cycle. This is done to avoid unintentional phase averaging which could occur since the maximum trigger rate is on the order of the rotation rate.

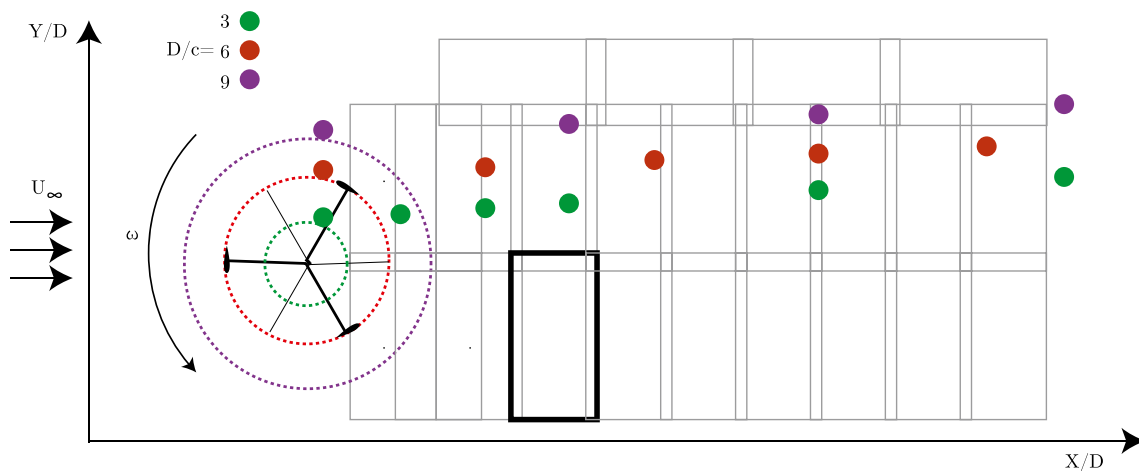


Fig. 3 The turbines' swept paths are outlined with struts and blades shown for the $D/c = 6$ model. Each rectangle represents a field of view for single data run using the two cameras. Overlapping fields of view are used to construct the large x - and y - velocity component

flow field. Inside the $D/c = 9$ turbine, fields of view were adjusted to image just downstream of the turbine to avoid any reflection issues. Hotwire measurement positions are shown by a dot color matched to each turbine model

A total of 360 images are used spanning the entire cycle for the time-averaged results.

The combination of phase averaging and time averaging accrues a large amount of data. For phase averaging (2 cameras \times 250 image pairs \times 20 fields of view \times 10 phases) = 100,000 images pairs were taken for each configuration. The data are processed using Davis software. Image pre-processing is done to remove any constant light sources in view and to normalize the data. Then the cross correlation is calculated using the GPU with square interrogation windows and multiple passes of decreasing size from 128 to 64 pixels with 50% overlap.

2.3 Constant temperature anemometry

Constant temperature anemometry (CTA) or “hotwire” data is collected in select locations based on the PIV data. The hotwire is a single channel compact MiniCTA system (Dantec Dynamics, Holtville, NY, USA). The output frequency is 10,000 Hz, in a range from 0–5 V. The hotwire data is recorded using Labview and is stamped with the turbine position from the encoder. This allows the output to be given as time, position, and voltage. The corresponding velocity is calibrated using the tunnel calibration and is fitted with a high-order polynomial fit.

The hotwire probe was placed at multiple locations, as shown in Fig. 3. The positions are normalized based on the turbine diameter. At each position, a series of runs are taken over the range of parameter shown in Table 1. Varying the tip-speed ratio allowed for a wide variation of dynamic solidities to be tested for each turbine. For each case, data was recorded for 120 s, corresponding to approximately 400–2000 cycles. The recordings are long enough to capture a large number of cycles at higher tip-speed ratio because we are also looking for common lower frequency content for all cases. The data is processed using Matlab to evaluate the frequency content in the flow. A low pass frequency filter, set at 2 kHz, is used to reduce the noise beyond the scope of the frequencies we are investigating. The spectral analysis is done using 8 symmetric Hanning windows, on the order of 1×10^5 , with 50% overlap.

The hotwire allows for frequency analysis in the temporal domain. This is combined with the PIV data, which yields a large spatial domain, to give a more complete picture of the phenomena in the flow.

3 Results and discussion

3.1 Time averaged flow fields

Ensemble averages of the flowfields behind three turbines are shown in Fig. 4. These give a sense of the overall shape

of the wake. We see the asymmetric wake that is typical of VAWTs (Araya and Dabiri 2015; Howell et al. 2010; Posa et al. 2016). Because we are using turbines of different D/c , the Reynolds number based on chord, Re_c , and the Reynolds number based on turbine diameter, Re_D cannot be held constant simultaneously. Here, we choose to keep the Reynolds number based on chord length constant. We vary the D/c ratio by changing the strut length, which means that the incoming flow velocity is constant for each case. Re_c was chosen to be constant because the wake vortices that are shed from the blades are on the scale of the chord length. While this creates a change in Re_D , the large-scale wake structure is not very sensitive to changes in this Reynolds number within this operational range, so this unavoidable change across models is not the driving parameter that affects the wake.

The fields of view must also be scaled based on either the chord length or diameter. The top row of Fig. 4 shows the full field of view taken scaled by chord length. This means the chord in each plot is the same length, and the x and y axes of the plots show the same range based on chord. This view is the same across cases because it is the full field captured during PIV in the wind tunnel. To normalize the scales based on the diameter, the fields from the lower D/c ratios, 6 and 3, are enlarged to match the scale of $D/c = 9$. These plots are shown on the bottom of Fig. 4, with their outline mapped by the dash-dot rectangle on the corresponding fields above. Note for the case $D/c = 9$, these fields are the same.

With a tip-speed ratio of $\lambda = 1.3$ and flow speed held constant for each case, the geometric solidity is driving the change in the wake. In previous work, the geometric solidity was varied among different turbine models by changing the number of blades while keeping the diameter the same (Araya et al. 2017). Here the D/c ratio is varied to change the geometric solidity in a different way, namely, by fixing the blade chord and changing the diameter of the turbine. Since a change in D/c also corresponds to a change in dynamic solidity, as earlier defined, this parameter is used for comparison in the discussion of the results. Qualitatively similar results are seen in the time average flow profiles by changing the dynamic solidity in different manners. In Fig. 5 we see that as the dynamic solidity increases, the blockage of the turbine results in a larger momentum deficit in the wake. Additionally, at lower dynamic solidities we see bands of velocity deficits as an artifact of the corresponding vortex structures that advect directly behind the turbine into the wake. In the high dynamic solidity case, we see an area of time-averaged flow reversal behind the turbine. These results are similar to those seen by increasing the tip-speed ratio, but here the tip-speed ratio is constant and the physical geometry is the only parameter that is varied.

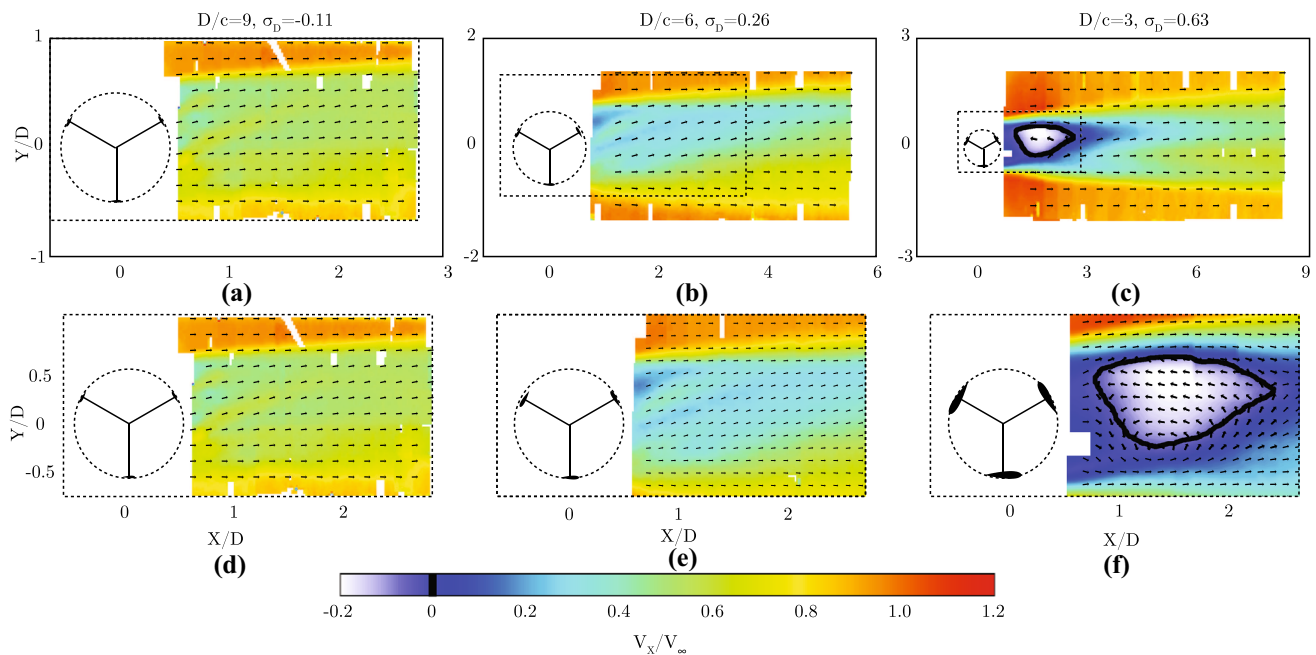


Fig. 4 Time averaged streamwise velocity fields are shown with vector arrows showing flow direction. This is done for three different D/c ratios, $D/c = 9$, $D/c = 6$, $D/c = 3$. The Reynolds number, $Re_c = 16.67$, and tip-speed ratio, $\lambda = 1.3$, are constant, giving dynamic solidities of $\sigma_D = -0.11$, $\sigma_D = 0.26$, and $\sigma_D = 0.63$. The flow is from left to right with the turbines' swept paths outlined and the direction of rotation is counter-clockwise. The struts and blades are

shown to give relative size, however, because these results are time averaged throughout the entire cycle, the position is arbitrary. The top row shows the entire field of view taken behind the turbine. The bottom row shows the same results normalized by turbine diameter. For the high solidity case, $D/c = 3$, an area of averaged reverse flow is seen and outlined in black

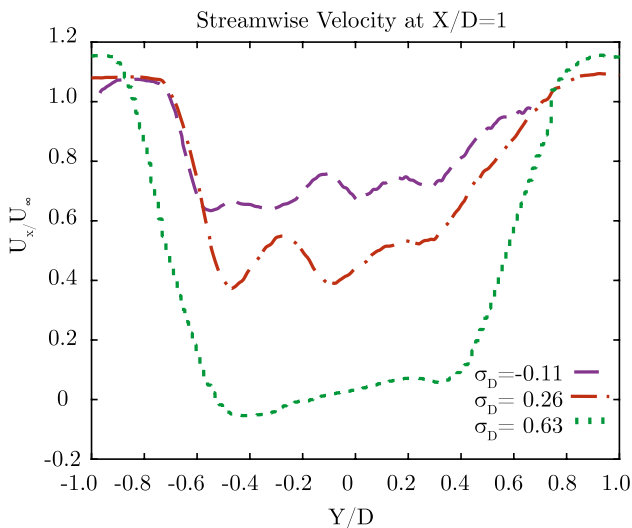


Fig. 5 The time averaged streamwise velocity profiles are plotted across $X/D = 1$. This is done for $D/c = 9$, $D/c = 6$, $D/c = 3$ with the position normalized by diameter (D). The deficit increases between the turbines as the geometric solidity increases. In the most solid case, $D/c = 3$, we see an area of averaged flow reversal behind the turbine

3.2 Phase averaged flow fields

Due to the cyclic nature of the turbine motion, the data are phase averaged based on the angular location of the blade. Here, 250 instances yield a single field. Because the turbine is symmetric about the axis of rotation, one-third of a cycle is imaged at 12 phases in 10° increments.

Figure 6 shows the same test cases that are seen in the time-averaged results of Fig. 4. Again, three different dynamic solidities are achieved by varying the D/c ratio while maintaining a constant tip-speed ratio, λ , and constant chord-based Reynolds number, Re_c . The turbine is rotating counterclockwise with the flow from left to right, and was imaged at the midplane, normal to the freestream velocity. In Fig. 6, one instance of the turbine's position is shown. The phase here is forward 20° from the upstream blade being normal to the freestream.

To identify the vortices in the wake, we use the swirling strength, λ_{ci} (Zhou et al. 1999). This is the imaginary part of the complex eigenvalues of the velocity gradient tensor. This method isolates the swirling component from stretching along the direction of the local flow. Then the magnitude of the swirling strength is artificially signed

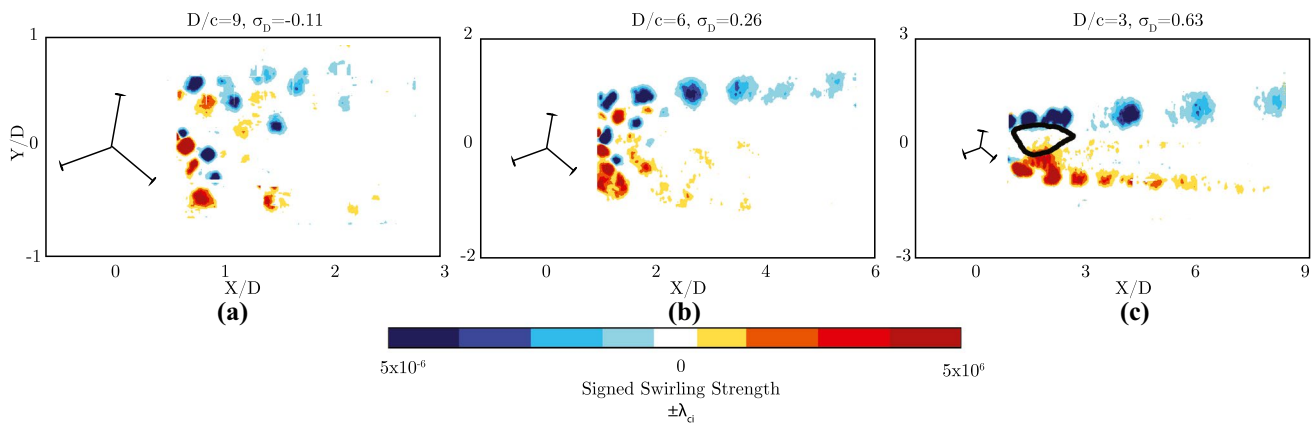


Fig. 6 The phase average swirling strength is plotted for each variation of D/c . The sign of the swirling strength is determined by the vorticity at that point with positive vorticity shown in red and neg-

ative shown in blue. The flow is from left to right with the turbine rotating counterclockwise. A single representative phase is plotted at the shown turbine position

by filtering out areas of negative vorticity and assigning the magnitude of the swirling strength in that region to be negative. This process labels each region of the appropriate direction of rotation and allows vortex pairs of opposite sign to be seen.

For fixed geometric solidity (σ), small values of the tip-speed ratio (λ) can lead to negative values of the dynamic solidity (σ_D) and will in fact diverge toward negative infinity as λ becomes close to zero. The same is true for fixed λ and small values of σ . The physical interpretation of σ_D is of how “solid” the turbine appears to the flow relative to a stationary cylinder of the same diameter and height. Thus, one physical interpretation of negative values for σ_D are the conditions where this cylinder and turbine analogy breaks down. We see some qualitative indication of this trend in Fig. 6. Specifically, for $\sigma_D = -0.11$ ($D/c = 9$), the vortices shed from the blades interact in the near wake, whereas for $\sigma_D = 0.63$ ($D/c = 3$) there is a clear line of vortices shed on either side of the wake, similar to that of a bluff body.

For the lower D/c cases, we see vortex pairs being shed into the near region of the wake. These vortices move along a diagonal path, downstream and toward the windward side of the wake. These paths can be seen in Fig. 4 as well by looking at the striping pattern created by the paths in the time-averaged results. These pairs of shed vortices do not propagate far downstream and either dissipate within two turbine diameters or are destroyed at the edge of the wake by the vortex chain shed on the windward side. This is consistent with previous work, where low and moderate tip-speed ratios result in similar low to moderate dynamic solidity with similar results.

For decreasing D/c from right to left in Fig. 6, the wake profile changes to a vortex line shed down both sides of the wake. This, like increasing the dynamic solidity by increasing tip-speed ratio, creates a steeper velocity gradient on

the proceeding side of the turbine compared with the lower solidity cases.

3.3 Temporal flow results

To analyze the temporal characteristics of the wake, a hotwire system is used at specific points in the shear layer (see Fig. 3 for measurement locations). The points were determined using PIV data (Fig. 4) and moving at set intervals downstream along a line of maximum shear. The parameter space for the hotwire data are shown in Fig. 2 and encompass a larger range than that of the PIV measurements. The hotwire system allows for sampling at 10 kHz while PIV data is limited to 25 Hz. The samples were taken at 10 kHz for 150 s. The spectral analysis is done using 8 symmetric Hanning windows, on the order of 1×10^5 , with 50% overlap. This spectra shows the vortex shedding captured at the blade passing frequency that was seen in Fig. 6 and, in some cases, other structures of different sizes in the wake. Additionally, by testing a range of dynamic solidities, the magnitude of the vortex chain created at the blade passing frequency can be compared across cases.

Figure 7 shows characteristic power spectra and phase-averaged profiles seen across the measured parameter space. These cases are different then the PIV results shown before in Fig. 6, and instead span a wider range of dynamic solidity to capture results where no frequency peak is seen. The top row shows the power spectra with the frequency normalized by the rotation rate of the turbine. With a three-bladed turbine, this gives a normalized blade passing frequency of 3 on the x -axis. The bottom row shows the relative to average, phase averaged velocity as a function of phase angle. The grey bands represent the margin of error for each plot. The error estimate for the power spectra is the 95% confidence bounds and for the phase results it is the standard deviation

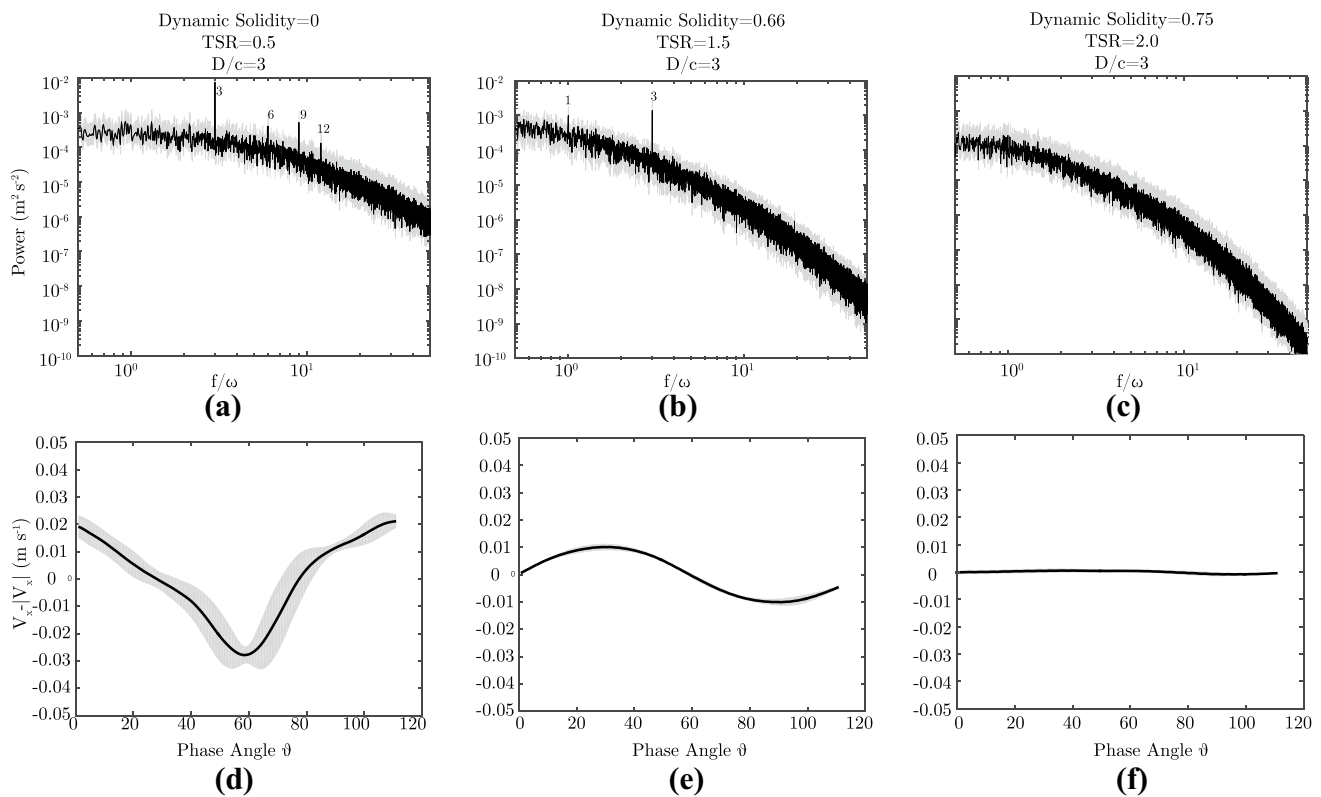


Fig. 7 The power spectra and phase averaged velocity profiles are shown for three cases. The frequency has been normalized by the turbines' rotational rate ω so that the blade passing frequency $f/\omega = 3$. Characteristic plots show different regimes characteristic of most cases. There are distinct differences between the power spectra in

these cases. On the left multiple spectra peaks are seen, the center case has one dominant peak at the blade passing frequency, and on the right, no dominant frequency is seen. The bottom row shows the phase averaged velocity profiles for the corresponding power spectra

of the samples at each position. The results in Fig. 7 are taken in the shear layer at the position of $X/D = 1$. For each case shown, the Reynolds number $Re_c = 16.66 \times 10^5$ is constant. Three cases are shown here for $D/c = 3$ with varied tip-speed ratios, as they represent three different characterizations seen across the entire parameter space.

In the center, Fig. 7b, we see a common case of a dominant peak at the blade passing frequency $f/\omega = 3$ with an additional peak at the turbine's rotation frequency $f/\omega = 1$. We don't see other peaks or indications of other common structures in the wake. The phase averaged profiles, below in Fig. 7e, show this for frequencies related to the rotation of the turbine. For this case, a single distinct velocity oscillation is seen at the blade passing frequency. This signature is characteristic of a single, distinct vortical structure being shed from each blade and advecting past the measurement point. The vortices being shed can be identified in the phase averaged PIV plots (Fig. 6) as the negatively signed vortex chain in the shear layer.

On the left, Fig. 7a, multiple peaks are seen in the frequency spectra. Looking at the phase averaged profile, Fig. 7d, we again see a strong peak at the blade passing

frequency. However the signal looks less like a simple sinusoid. Compared to Fig. 7e there is additional frequency content. Looking at the phase-averaged PIV data, Fig. 6, this profile would correspond to an instance where the vortex chain in the wake is also being interrupted by other shed vortices moving against the shear layer. An example can be seen in Fig. 6b, where vortices shed earlier by the blades progression on the retreating side advect into the top shear layer. This combination of a strong chain of vortices shed into the shear layer, and additional vortices propagating into the shear layer, gives rise to the harmonics seen.

No dominant frequency is seen in Fig. 7c. The blade passing frequency does not produce a peak and no structures outside a normal variation are seen in the wake. In Fig. 7f the velocity fluctuations have no distinctive variation in phase with the turbine.

At a fixed X/D location, there is a correlation between high dynamic solidity and blade passing frequency when compared to low and negative dynamic solidity cases. This is explored further in Fig. 8. However, there is seemingly no rule when comparing a single peak to multiple peaks. The

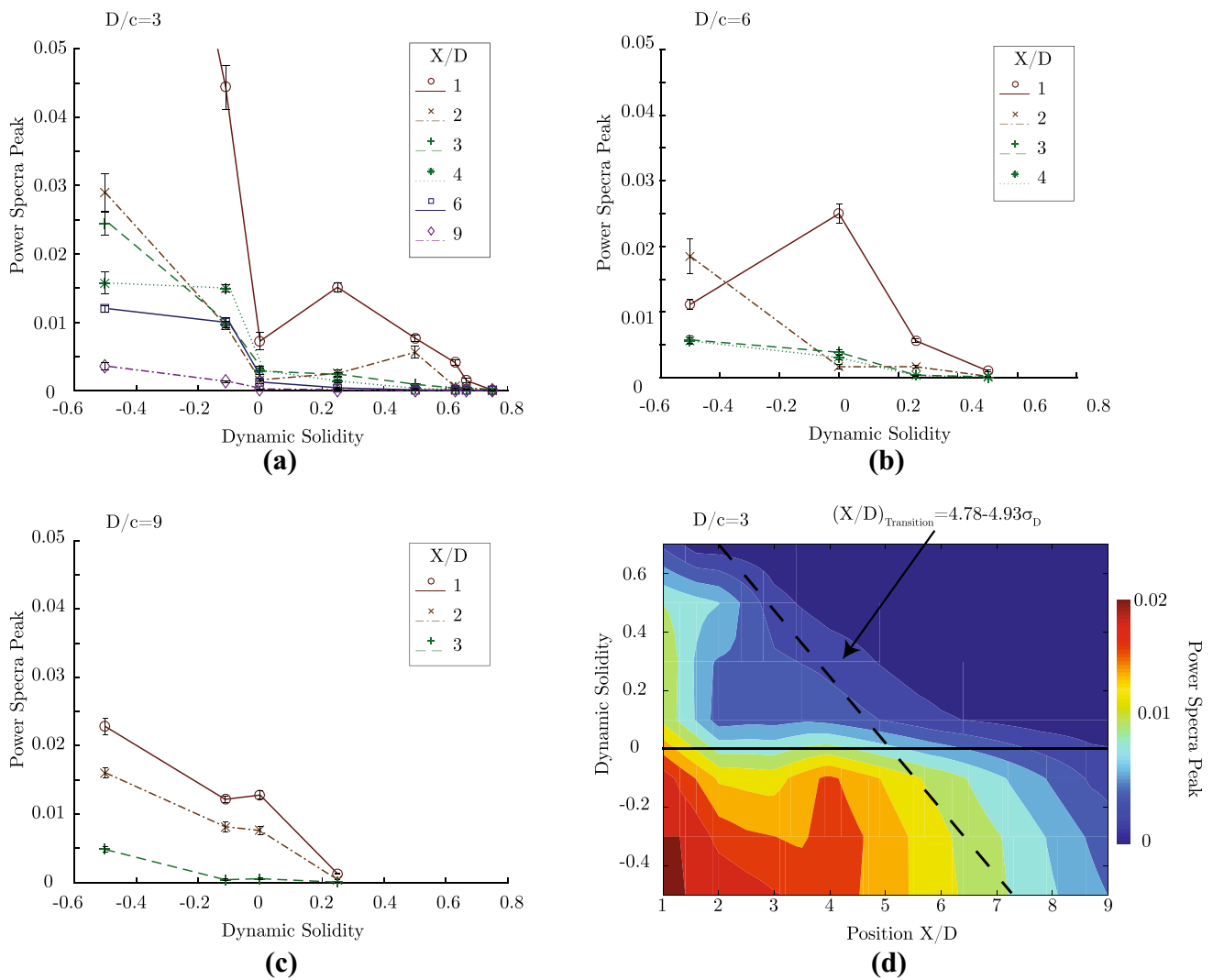


Fig. 8 The amplitude of the power spectra peak at the blade passing frequency is plotted against dynamic solidity. Progressing across and down, from a to c, this is done for each turbine $D/c = 3, 6, 9$. Each

line shows a single position downstream. Plot d, shows the average magnitude mapped across the entire experimental parameter space for $D/c = 3$

timing and influence is more sensitive so that no obvious relationship between dynamic solidity and number of peaks can yet be determined.

Figure 8 shows the power spectra peak at the blade passing frequency. There is a decay in the peak amplitude moving downstream in the wake. By looking along the x-axis of Fig. 8d, we see a decrease in the signal peak—as you would expect in an energized turbulent and viscous flow, such as grid turbulence. However, in addition to the simple decay, we see that when dynamic solidity increases, this decay is much more rapid. For lower dynamic solidity, the vortex peak can persist for multiple diameters downstream, but, at higher cases the peak decays rapidly.

Along the y-axis there is a trend that the magnitude of the blade passing frequency response decreases as the dynamic solidity increases. While this is not a monotonic effect, the

physics of this phenomenon is clearly more complex than to collapse on a single non-dimensional parameter, the trend is present for each turbine geometry, and, as Fig. 8d shows, across geometries. This is also shown for each turbine in Fig. 8a–c by moving along each line of increasing dynamic solidity. In addition to this decay, above a certain dynamic solidity the blade passing frequency disappears entirely.

In Fig. 8a the spectra peak is plotted along lines of constant dynamic solidity for the $c/D = 3$ turbine. Figure 8b, c show the same for $c/D = 6$ and 9. Instead of the averaged values being mapped across multiple cases, every case is shown. Each X/D location is plotted in Fig. 8a–c in a different color. We see the same trend stated before: by increasing the dynamic solidity, the power spectra content at the blade passing frequency decays. Additionally, we see that this trend is closely linked to the dynamic solidity. This shows

that the metric of dynamic solidity is a good indicator of this phenomenon, normalizing the tip-speed ratio across different physically solid turbines.

3.4 Vortex dynamics

The changes in the prominence and persistence of the blade passing frequency in the wake may be due to the spacing and intensity of the vortices shed into the shear layer. At low dynamic solidity, the spacing between vortices is large, so there is little interaction or dissipation between the vortices to distort the chain shed at the blade passing frequency. At very low to negative dynamic solidity, this periodic signal may be distorted due to the presence of vortices of opposite sign traveling freely in the near wake. However, at high dynamic solidity the vortex chain is compressed such that the individual vortices shed from each blade are distorted as they interact in the near wake, leading to a weaker signal at the blade passing frequency. This effect may be exaggerated further downstream as an isolated vortex in the wake will persist. However, when the spacing is closer, vortex merging may take place and distort the flow sooner. After this transition from the dominant blade passing frequency, Araya et al. (2017), showed a bluff body like shedding would occur. However, lack of sufficient runs after this transition prevents us from discussing this in this paper.

4 Conclusions

Wind tunnel testing of multiple VAWT models show distinct wake changes that correspond to changes in dynamic solidity. Previous work suggests that changing the tip-speed ratio leads to substantial wake variation and this may be because changing the tip-speed ratio changes the dynamic solidity. In this work, we achieve a similar change in dynamic solidity by varying the D/c ratio and holding the tip-speed ratio constant. This change leads to very similar characteristic shifts in the wake such as a greater blockage effect, including averaged flow reversal in the case of high dynamic solidity ($D/c = 3$). The wake profiles are also dependent on dynamic solidity with steeper gradients on the retreating side of the wake for high dynamic solidity cases.

The phase-averaged vortex identification shows that both the blockage effect and the wake structures are similarly affected by a change in dynamic solidity. At lower dynamic solidity, pairs of vortices are shed into the wake directly downstream of the turbine. For all three models, a vortex chain is shed into the shear layer at the edge of the wake where the blade is processing into the freestream.

Using PIV data as a guide, point velocity measurements are taken along the shear layer to investigate the frequency content in the edge of the wake. Different dynamic solidity values produce different characteristic power spectra in the

wake: a distinctive peak at the blade passing frequency, multiple peaks, or no peaks. The relationship between dynamic solidity and the vortex shedding show a trend of a decreasing tendency for distinct vortices in the wake with increasing dynamic solidity; instead, we begin to see a constant shear layer. Additionally, the distinctive structures seen at lower dynamic solidity persist further downstream.

These changes help to confirm that dynamic solidity is a useful design parameter that includes both physical solidity variation as well as tip-speed ratio to estimate the wake profile based on its effective blockage. These changes were seen in the vortex shedding and the frequency content in the shear layer. More detailed analysis is needed to see the exact wake profile relating all of the vortex shedding in the wake. However, for many wake characteristics, dynamic solidity captures fundamental changes independent of a change to the dynamic parameter—tip-speed ratio—or physical parameter—the solidity in the form of the D/c ratio.

Acknowledgements The authors wish to thank Raymond Hummels and Allen Schultz for their experimental assistance. Thank you to The Metro Washington Chapter of the Achievement Rewards for College Students (ARCS) Foundation and the McNichols Foundation for their financial support of Colin Parker. Thank you to the George Washington Center for Biomimetics and Bioinspired Engineering (COBRE) for the use of facilities.

References

- Ainslie JF (1988) Calculating the flowfield in the wake of wind turbines. *J Wind Eng Ind Aerodyn* 27:213–224
- Araya DB, Dabiri JO (2015) A comparison of wake measurements in motor-driven and flow-driven turbine experiments. *Exp Fluids* 56(7):1–15
- Araya DB, Colonius T, Dabiri JO (2017) Transition to bluff-body dynamics in the wake of vertical-axis wind turbines. *J Fluid Mech* 813:346–1120
- Armstrong S, Fiedler A, Tullis S (2012) Flow separation on a high Reynolds number, high solidity vertical axis wind turbine with straight and canted blades and canted blades with fences. *Renew Energy* 41:13–22. <https://doi.org/10.1016/j.renene.2011.09.002>
- Barsky DA, Posa A, Rahromostaqim M, Leftwich M, Balaras E (2014) Experimental and computational wake characterization of a vertical axis wind turbine. 32nd AIAA applied aerodynamics conference. Atlanta, GA
- Barthelme RJ, Rathmann O, Frandsen ST, Hansen KS, Politis E, Prospathopoulos J, Rados K, Cabezón D, Schlez W, Phillips J, Neubert A, Schepers JG, Pijl SPVD (2007) Modelling and measurements of wakes in large wind farms. *J Phys Conf Ser* 75(012):049. <https://doi.org/10.1088/1742-6596/75/1/012049>
- Battisti L, Zanne L, Dell'Anna S, Dossena V, Persico G, Paradiso B (2011) Aerodynamic measurements on a vertical axis wind turbine in a large scale wind tunnel. *J Energy Resour Technol* 133(3):031,201. <https://doi.org/10.1115/1.4004360>
- Bianchini A, Ferrara G, Ferrari L (2015) Design guidelines for H-Darrieus wind turbines: optimization of the annual energy yield. *Energy Convers Manag* 89:690–707. <https://doi.org/10.1016/j.enconman.2014.10.038>

- Brusca S, Lanzafame R, Messina ÁM (2014) Design of a vertical-axis wind turbine: how the aspect ratio affects the turbine's performance. *Int J Energy Environ Eng* 5:333–340. <https://doi.org/10.1007/s40095-014-0129-x>
- Cal R, Lebrón J, Castillo L (2010) Experimental study of the horizontally averaged flow structure in a model wind-turbine array boundary layer. *J Renew Sustain Energy* 2(1):013,106. <https://doi.org/10.1063/1.3289735>
- Calaf M, Meneveau C, Meyers J (2010) Large eddy simulation study of fully developed wind-turbine array boundary layers. *Phys Fluids* 22(1):015110. <https://doi.org/10.1063/1.3291077>
- Chamorro LP, Hill C, Morton S, Ellis C, Arndt REA, Sotiropoulos F (2013) On the interaction between a turbulent open channel flow and an axial-flow turbine. *J Fluid Mech* 716(May):658–670. <https://doi.org/10.1017/jfm.2012.571>
- Dabiri JO (2011) Potential order-of-magnitude enhancement of wind farm power density via counter-rotating vertical-axis wind turbine arrays. *J Renew Sustain Energy* 3(4):043104. <https://doi.org/10.1063/1.3608170>
- Dunne R, McKeon BJ (2015) Dynamic stall on a pitching and surging airfoil. *Exp Fluids* 56(8):1–15. <https://doi.org/10.1007/s00348-015-2028-1>
- Edwards J, Danao L, Howell R (2015) PIV measurements and CFD simulation of the performance and flow physics and of a small-scale vertical axis wind turbine. *Wind Energy* 18(2):201–217. <https://doi.org/10.1002/we.1690>
- Howell R, Qin N, Edwards J, Durrani N (2010) Wind tunnel and numerical study of a small vertical axis wind turbine. *Renew Energy* 35(2):412–422
- Möllerström E, Larsson S, Ottermo F, Hylander J, Bååth L (2014) Noise propagation from a vertical axis wind turbine. In: *inter-noise*, pp 1–8
- Parker CM, Leftwich MC (2016) The effect of tip speed ratio on a vertical axis wind turbine at high Reynolds numbers. *Exp Fluids* 57(5):1–4864. <https://doi.org/10.1007/s00348-016-2155-3>
- Posa A, Parker CM, Leftwich MC, Balaras E (2016) Wake structure of a single vertical axis wind turbine. *Int J Heat Fluid Flow* 61:75–84. <https://doi.org/10.1016/j.ijheatfluidflow.2016.02.002>
- Roh SC, Kang SH (2013) Effects of a blade profile, the Reynolds number, and the solidity on the performance of a straight bladed vertical axis wind turbine. *J Mech Sci Technol* 27(11):3299–3307. <https://doi.org/10.1007/s12206-013-0852-x>
- Ryan KJ, Coletti F, Elkins CJ, Dabiri JO, Eaton JK (2016) Three-dimensional flow field around and downstream of a subscale model rotating vertical axis wind turbine. *Exp Fluids* 57(3):1–15. <https://doi.org/10.1007/s00348-016-2122-z>
- Simão Carlos F, Van Gijs K, Van Gerard B, Fulvio S (2009) Visualization by PIV of dynamic stall on a vertical axis wind turbine. *Exp Fluids* 46(1):97–108. <https://doi.org/10.1007/s00348-008-0543-z>
- Tescione G, Ragni D, He C, Simão Ferreira C, van Bussel G (2014) Near wake flow analysis of a vertical axis wind turbine by stereoscopic particle image velocimetry. *Renew Energy* 70:47–61. <https://doi.org/10.1016/j.renene.2014.02.042>
- Zhou J, Adrian RJ, Balachandar S, Kendall TM (1999) Mechanisms for generating coherent packets of hairpin vortices in channel flow. *J Fluid Mech* 387:353–396. <https://doi.org/10.1017/S002211209900467X>